Application of a Limiting Form of the Rényi Entropy for Molecular Imaging of Tumors Using a Clinically Relevant Protocol

J. N. Marsh, K. D. Wallace,
G. M. Lanza, S. A. Wickline, and M. S. Hughes
Washington University School of Medicine
Department of Internal Medicine
St. Louis, Missouri 63108
Email: jnm@cvu.wustl.edu

J. E. McCarthy
and M. V. Wickerhauser
Washington University in St. Louis
Department of Mathematics
St. Louis, Missouri 63130

Abstract—We demonstrate a novel approach to ultrasonic detection of molecularly targeted nanoparticle contrast agent accumulation in a xenographic mouse tumor model *in vivo*. This is accomplished by imaging the entire mouse tumor volume at 15-minute intervals following injection of $\alpha_v\beta_3$-targeted perfluoro-carbon core nanoparticles. Radiofrequency (RF) data were stored for off-line analysis using signal energy and a limiting form of the Rényi entropy suitable for real-time calculation, $I_{f,\infty}$. The results indicate that $I_{f,\infty}$ may be used to reliably detect accumulation of targeted nanoparticles within 15 minutes of injection without the need for image subtraction, whereas signal energy images showed less sensitivity to nanoparticle accumulation. The ability to detect nanoparticle accumulation without requiring image subtraction or fixing the transducer in place are necessary prerequisites for translation of this technology to the clinic.

I. INTRODUCTION

In previous studies we have demonstrated the utility of several different entropy quantities for molecular imaging of a nanoscale contrast agent suitable for magnetic resonance, X-ray, and ultrasound imaging of tumor neovasculature. In all of these studies, targeted nanoparticles were injected into an animal model and imaged ultrasonically as they accumulated at sites in the region of the growing front of the tumor.

Due to the sparseness of targeting sites, the small size of the nanoparticles, and the architecture of the neovascular bed, subresolution techniques are required for their detection. The approach we take here is based partly on the application of information-theoretic/thermodynamic quantities, in which these concepts are applied "up front" in a moving window analysis of digitized RF waveforms to form "information" images whose pixel values are determined by the value of entropy derived from the RF within the moving window [1]–[4].

Concurrent with these investigations we have pursued development of automated algorithms, based on image pixel value histograms, for segmentation of ensembles of images into "targeted" and "non-targeted" portions. The major criterion for these algorithms is that they not require image subtraction, since in many biological imaging applications slight movement of tissue between image acquisitions can lead to artificial enhancement of tissue boundaries in the field of view that are erroneously generated by the subtraction. A longer-term goal is that these algorithms perform robustly on data sets where the transducer is utilized in a clinically relevant manner; namely, that the transducer not be rigidly fixed in position during acquisition, as such a requirement is unlikely to be translated to the clinic.

II. MATERIALS AND METHODS

A. Entropy-Based Image Formation

We base our current study on the limiting form of the Rényi entropy, $I_{f,\infty}$, since this quantity is calculable in real time [3]. $I_{f,\infty}$ takes the form

$$I_{f,\infty} = \log\left[\sum_{\{t_k|f'(t_k)=0\}} \frac{1}{|f''(t_k)|}\right]. \qquad (1)$$

The logarithm of the signal energy is given by

$$\log[E_f] = \log\left[\sum_{i=0}^{N} f(t_i)^2\right], \qquad (2)$$

where N is the number of points in the moving window.

B. Nanoparticles for Molecular Imaging

Methods developed in our laboratory were used to prepare liquid perfluorocarbon emulsions (nominal size $200\pm30\mu m$) encapsulated by a lipid-surfactant monolayer. Targeting to $\alpha_v\beta_3$ integrins associated with tumor neovasculature was accomplished by incorporating an "Arg-Gly-Asp" pep-tidomimetic in the lipid layer.

C. Animal Model and Ultrasound Data Acquisition

Murine melanoma B16 cancer cells were implanted in the inguinal fat pad of 15 black mice (NCI C57BL/6N) between 19 and 20 days prior to acquisition of data. Mice were preanesthesitized and the area around the tumor was shaved
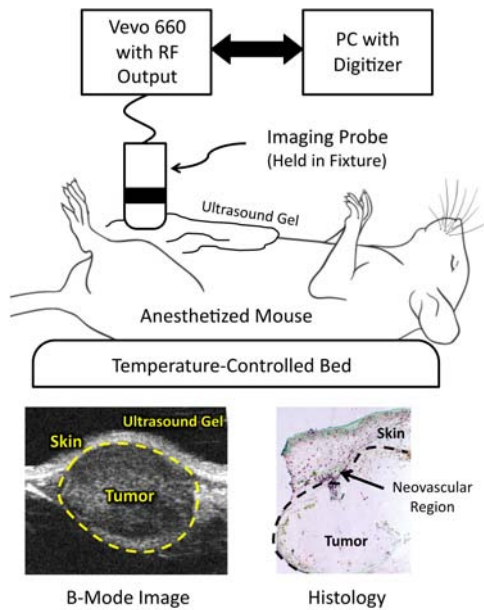
Fig. 1. Top: Equipment setup. Bottom left: Sample cross-sectional ultrasound image of B16 tumor. Bottom right: Histological stain for vessels (dark purple) in an excised tumor.

Fig. 2. Typical conventional grayscale (top), $I_{f,\infty}$ (middle), and $\log[E_f]$ images (bottom).

and cleaned. Each animal was then injected with either $\alpha_v\beta_3$-targeted nanoparticle emulsion (n=6), non-targeted nanoparticle emulsion (n=6), or saline (n=3) at a whole body dose of 1 mL/kg. Ultrasound gel was applied between the tumor and transducer to provide acoustic coupling. Subsequently, ultrasound data were acquired at 15-min. intervals for 1 hr.

A diagram of our apparatus is shown in Fig. 1. RF data were acquired with a research ultrasound system (Visualsonics Vevo 660 with 40 MHz probe) with analog RF output. RF data corresponding to single frames were digitized at 200 MHz and stored off-line. Each frame corresponded spatially to a region 1.0 cm wide and 0.8 cm deep, and consisted of 384 lines which were 2048 points long. The transducer was scanned over the length of the tumor in 100 μm steps. Scans occurred every 15 minutes (up to 1 hr) post-injection. A conventional ultrasound image from one of the tumors is shown in the bottom left part of Fig. 1. This cross-sectional view from the middle of the tumor area clearly shows the tumor capsule growing just under the skin surface. A histological section of a similar tumor is shown in the bottom right panel of the figure, indicating significant neovasculature between skin and tumor capsule.

D. Ultrasonic Data Processing

All RF data were lowpass filtered (high frequency cutoff at 36 MHz) to decrease noise levels and then processed according to two different schemes prior to preparation of conventional, $\log[E_f]$ or $I_{f,\infty}$ images. In the first, each RF line was upsampled to 4096 points using a simple cubic spline in order to improve the stability of the receiver algorithms. Next, a moving window analysis was performed on the second derivative data set (which is computed as part of the spline interpolation), using Eq. (1)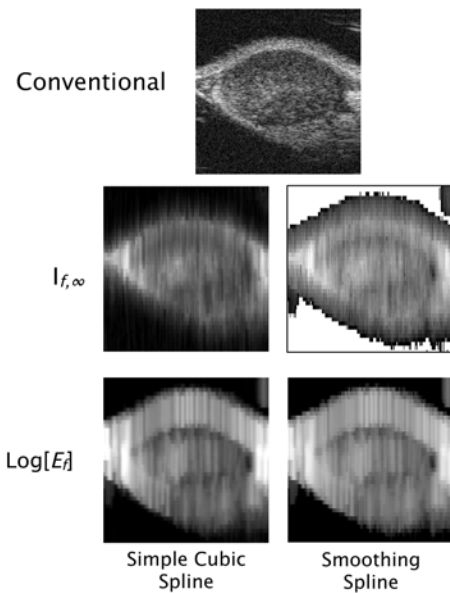 to compute $I_{f,\infty}$, by moving a rectangular window 1.28 μs long in 0.16 μs steps, resulting in 57 window output values for each RF line. In the second scheme, an optimal smoothing spline [5] was fit to the lowpass filtered data withing the moving window, and then a similar analysis was performed. Window length was chosen to optimize sensitivity, noise level and spatial resolution.

A representative set of these $\log[E_f]$, and $I_{f,\infty}$ images reconstructed from the same RF data representing a single frame is shown in Fig. 2. The top panel shows a conventional B-mode image, i.e., logarithm of the signal envelope of the backscattered RF. In the next row are two $I_{f,\infty}$ images produced from the same raw RF: images in the left column were made after fitting a simple cubic spline to the RF, while those in the right column were made using an optimal smoothing spline. Speckle is reduced, as well as spatial resolution, although structure internal to the tumor capsule is still evident. Additionally, the image produced using smoothing splines exhibits the suppression of noise-dominated portions of the image that we have previously observed [6], as indicated by the white region above the tumor and the distal portions of the image. In the bottom row are $\log[E_f]$ images made from the same RF and with the same preprocessing as the corresponding $I_{f,\infty}$ images. We note spatial resolution seems to be better preserved in the $I_{f,\infty}$ than the $\log[E_f]$ images.

E. Image Processing

Images such as those shown in Fig. 2 were prepared from RF data acquired for the entire tumor volumes at all time points. Histograms of pixel values were formed from each ensemble of images (either conventional, $\log[E_f]$, or $I_{f,\infty}$) and used to segment images at each time point. For $I_{f,\infty}$ computations, the mean value of the most negative 2% of pixels in the histogram of the image was computed, followed
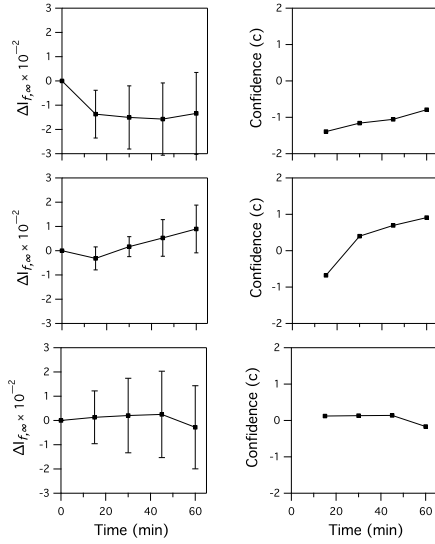
Fig. 3. Left column: Plots of the change in real-time entropy ($\Delta I_{f,\infty}$) images for each treatment group. Right column: corresponding confidence plots (Eq. (3)). These data were obtained for the CDF-threshold set to include the lower 12% of pixel values in the $I_{f,\infty}$ images in each group.

by the mean value of the most negative 4% of pixels in the image histogram, and so forth, up to 98% in increments of 2%. A similar histogram-based analysis was performed on $\log[E_f]$ images, using the most positive pixels values in similar 2% increments. For $I_{f,\infty}$ images at the appropriate threshold, these pixels were found to lie in a region between the tumor capsule and skin, consistent with previous studies [1], [2], [4] and also with physiologic constraints governing where the tumor is most likely to recruit neovasculature for its blood supply. Enhancement at a given threshold was computed as the change in mean value of receiver output (either $I_{f,\infty}$ or $\log[E_f]$) relative to the value immediately prior to injection. We emphasize that subtraction of these values after an averaging step, which renders them spatially independent, yields no danger of image artifacts induced by tissue motion.

III. RESULTS AND DISCUSSION

An example of the time course of the change of the mean pixel values (with standard error bars) for $I_{f,\infty}$ images segmented by setting the CDF-threshold to include only the bottom 12% of $\Delta I_{f,\infty}$ pixel values of the central 20 frames is shown in the left column of Fig. 3. The right column shows the time course plots of "confidence" Eq. (3), discussed below. The control group injected with non-targeted nanoparticles exhibits a significant positive change over time post-injection, although the magnitude of "confidence", quantified by Eq. (3), is less than that achieved using $\alpha_v\beta_3$-targeted nanoparticles at earlier time points. The second control group, injected with saline, exhibits no significant change with time.

For the purposes of detection, it is actually the ratio of the mean value to the standard error that is significant. To shorten subsequent discussion of our results we will define this ratio
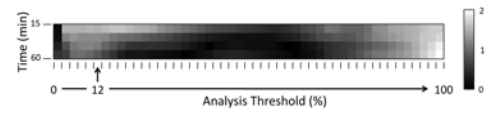

Fig. 4. Confidence magnitude values, $|\mathbf{c}|$ (Eq. (3)), in image format, for the group injected with $\alpha_v\beta_3$-targeted nanoparticles. Pixel values of the 12% column in this image correspond to the data shown in the top panel of Fig. 3.

as the confidence, $\mathbf{c}$, where

$$\mathbf{c} = \frac{mean}{standard\ error}. \qquad (3)$$

Plots of this quantity for each group are shown in the right hand column of Fig. 3. We see from Fig. 3 that only the group injected with $\alpha_v\beta_3$-targeted nanoparticles exhibits a significant change in $I_{f,\infty}$ at or before the 30-min. time point, as evident from confidence values $|\mathbf{c}| \geq 1$. As the left column of the figure shows, this is due to a combination of the larger change in mean value and smaller standard error in the "targeted" versus control groups.

Fig. 4 shows $|\mathbf{c}|$ for the $\alpha_v\beta_3$-targeted group for times at 15, 30, 45 and 60 min. post-injection at all analysis-thresholds between 0 to 98% (in 2% increments). The $|\mathbf{c}|$ values are rendered in gray scale. The analysis-threshold value corresponding to the data in the right hand column of Fig. 4 is indicated by arrow and labeled by 12%. Panels of this type were prepared for all experimental groups in our study using both $I_{f,\infty}$ and $\log[E_f]$ images.

Fig. 5 is comprised of several of these confidence panels, all obtained using smoothing splines in the data analysis. All panels have been "binarized" by representing confidence values with absolute value less than one by black pixels, while values with magnitude greater than one are shown in white. The top portion of the figure shows three panels obtained using $I_{f,\infty}$ images, arranged as: (top) the group injected with $\alpha_v\beta_3$-targeted nanoparticles (corresponding to a binary version of Fig. 4, (middle) animals injected with non-targeted nanoparticles, and (bottom) animals given saline. Gray bars have been drawn on the image to separate the panels visually. In the bottom half of the figure are the corresponding panels obtained using $\log[E_f]$ images. The $I_{f,\infty}$ panels are noteworthy in that the top line of the targeted group (corresponding to 15 min. post-injection) is white for all analysis thresholds between 4 and 32%, while the bottom panels are black in the top line for nearly all thresholds, suggesting that a choice of analysis thresholds anywhere in this range would correctly separate the targeted group from the two control groups at this time point. Interestingly, the middle panel indicates some sensitivity of $I_{f,\infty}$ to accumulation of non-targeted nanoparticles for analysis thresholds between 28% to 68%, at times greater than or equal to 30 min. post-injection.

A similar comparison of binarized confidence values for $I_{f,\infty}$ obtained from simple cubic vs. smoothing spline preprocessing (not shown) indicates that their performance is roughly equivalent, with a slight operational advantage being offered by the smoothing spline analysis, as it yields a slightly larger
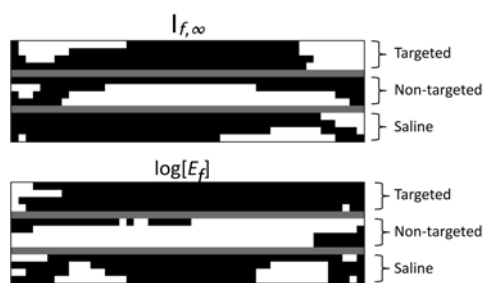
Fig. 5. Confidence values, $|\mathbf{c}|$ (Eq. (3)), for the average change in either $I_{f,\infty}$ (top half) or $\log[E_f]$ (bottom half) relative to zero time, at 15, 30, 45, and 60 min. post-injection for all thresholds in each experimental group. Confidence magnitude values less than one are represented by black pixels, values above one are white. These results were obtained using optimal smoothing splines. The top $I_{f,\infty}$ panel corresponds to a binarized version of Fig. 4.

regime of analysis thresholds where the targeted group is separated from both control groups at earlier times. Consequently, we will limit subsequent discussion to results obtained using smoothing splines.

The second panel from the top of Fig. 6 is the same as shown in the top of Fig. 5. The remaining panels were obtained by $I_{f,\infty}$ analysis when selecting differing numbers of frames from each data set. We observe that the "Middle 20 Frames" panel exhibits the largest contiguous area for which the $\alpha_v\beta_3$-targeted animals exhibit a positive result (i.e. white area) without corresponding false positive results in either control group (i.e. 4% to 32% range at 15 min., and 8% to 12% range at 15-60 min). In the lower three panels, the variation in the size of contiguous white regions becomes greater, as might be expected with smaller acquired dataset sizes. In contrast, when selecting all frames in the acquired dataset, the threshold range associated with positive results for the targeted group and no false positives in the control groups is quite small (2% to 4% at 15 min). This is likely due to the inclusion of non-cancerous tissue at the edges of the tumors with fewer $\alpha_v\beta_3$ binding sites. Note also the difference between the bottom two panels, which differ only in the single frame chosen for analysis; the instability seen in the amount of false positives associated with the saline groups establishes that single frame data sets acquired in the scanned acquisition mode are unsuitable for detection of targeted nanoparticles in this animal model.

The main result of this study is that it is possible to detect accumulation of targeted nanoparticles in a clinically relevant time frame (15 min.), using an automated image segmentation algorithm that does not require image subtraction, and which operates on raw RF acquired using a scanned-frame acquisition protocol. The entirely automated nature of the analysis protocol, culminating in the "targeted" vs. "non-targeted" decision point, is relevant for application of these techniques to the emerging generation of clinical devices intended for point-of-care application.
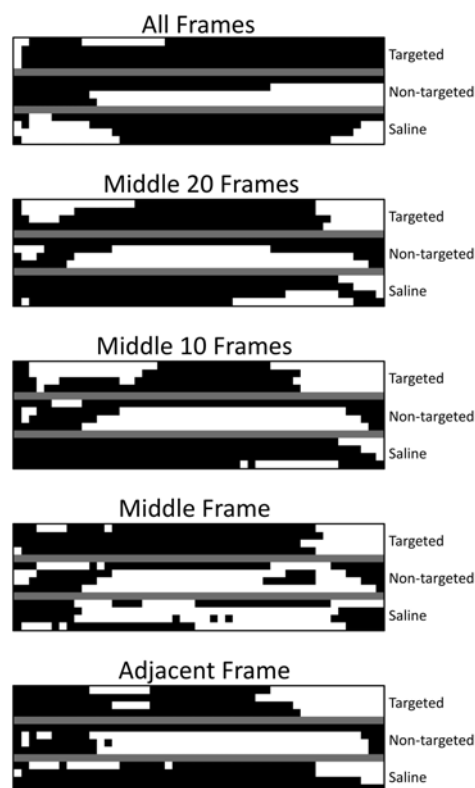
Fig. 6. A comparison of the thresholded ($|\mathbf{c}| < 1 \rightarrow$ black, $|\mathbf{c}| \geq 1 \rightarrow$ white) $I_{f,\infty}$ confidence images for all three groups in our study, obtained using subsets of the entire data set as indicated.

REFERENCES

[1] M. S. Hughes, J. E. McCarthy, J. N. Marsh, J. M. Arbeit, R. G. Neumann, R. W. Fuhrhop, K. D. Wallace, D. R. Znidersic, B. N. Maurizi, S. L. Baldwin, G. M. Lanza, and S. A. Wickline, "Properties of an entropy-based signal receiver with an application to ultrasonic molecular imaging." *J Acoust Soc Am*, vol. 121, no. 6, pp. 3542–3557, Jun 2007.

[2] M. S. Hughes, J. N. Marsh, J. M. Arbeit, R. G. Neumann, R. W. Fuhrhop, K. D. Wallace, L. Thomas, J. Smith, K. Agyem, G. M. Lanza, S. A. Wickline, and J. E. McCarthy, "Application of renyi entropy for ultrasonic molecular imaging." *J Acoust Soc Am*, vol. 125, no. 5, pp. 3141–3145, May 2009.

[3] M. S. Hughes, J. E. McCarthy, M. V. Wickerhauser, J. N. Marsh, J. M. Arbeit, R. W. Fuhrhop, K. D. Wallace, T. Thomas, J. Smith, K. Agyem, G. M. Lanza, and S. A. Wickline, "Real-time calculation of a limiting form of the renyi entropy applied to detection of subtle changes in scattering architecture." *J Acoust Soc Am*, vol. 126, no. 5, pp. 2350–2358, Nov 2009.

[4] J. N. Marsh, K. D. Wallace, J. E. McCarthy, M. V. Wickerhauser, B. N. Maurizi, G. M. Lanza, S. A. Wickline, and M. S. Hughes, "Application of a real-time, calculable limiting form of the renyi entropy for molecular imaging of tumors," *IEEE Trans Ultrason Ferroelec Freq Control*, vol. (in press), 2010.

[5] C. H. Reinsch, "Smoothing by spline functions," *Numerische Mathematik*, vol. 10, pp. 177–183, 1967.

[6] M. S. Hughes, J. N. Marsh, J. E. McCarthy, B. Wickerhauser, R. W. Maurizi, K. D. Wallace, G. M. Lanza, and S. A. Wickline, "Molecular imaging of tumors using an improved calculation of a limiting form of renyi entropy based on smoothing splines," *I.E.E.E. Transactions on Medical Imaging*, vol. (in review), 2010.